inorganics

MDPI

Article

Investigation of the Reduction of a Molybdenum/Iron Molecular Nanocluster Single Source Precursor

Gibran L. Esquenazi [1] and Andrew R. Barron [1,2,3,*]

[1] Department of Chemistry, Rice University, Houston, TX 77005, USA; gle1@rice.edu
[2] Department of Materials Science and Nanoengineering, Rice University, Houston, TX 77005, USA
[3] Energy Safety Research Institute, Swansea University Bay Campus, Swansea SA1 8EN, UK
* Correspondence: arb@rice.edu or a.r.barron@swansea.ac.uk; Tel.: +1-713-348-5610

Received: 15 July 2018; Accepted: 25 September 2018; Published: 27 September 2018

Abstract: The thermolysis of the polyoxometalate cluster $[H_xPMo_{12}O_{40} \subset H_4Mo_{72}Fe_{30}(O_2CMe)_{15}O_{254}(H_2O)_{90-y}(EtOH)_y]$ (**1**) under air, argon, and reducing conditions (5%, 10%, 50% H_2 with Ar balance) has been investigated. The resulting products have been characterized by XRD, SEM, and EDX analysis. Thermolysis in air at 1100 °C yields predominantly Fe_2O_3, due to sublimation of the molybdenum component; however, under Ar atmosphere, the mixed metal oxide ($Fe_2Mo_3O_8$) is formed along with Mo and MoO_2. Introduction of 5% H_2 (1100 °C) results in the alloy Fe_2Mo_3 in addition to $Fe_2Mo_3O_8$ and Mo; in contrast, reduction at a lower temperature (900 °C) yields the carbide (Fe_3Mo_3C) and the analogous oxide (Fe_3Mo_3O), suggesting that these are direct precursors of Fe_2Mo_3. Increasing the H_2 concentration (10%) promotes carbide rather than oxide formation (Fe_3Mo_3C and Mo_2C), until alloy formation ($Fe_{7.92}Mo_{5.08}$) predominates under 50% H_2 at 1200 °C. The effect of temperature and H_2 concentration on the composition, grain size, and morphology has been investigated by EDX, SEM, and XRD. The relationship of the composition of **1** (i.e., Fe:Mo = 30:84) with the product distribution is discussed.

Keywords: mixed metal oxide; polyoxometalate; nanocluster; nanoalloys

1. Introduction

The concept of a single source precursor for materials synthesis evolved in the 1980s as a chemical route to a range of materials, from oxides to semiconductors [1–3]. Initial approaches involved simply incorporating the elements required in the product into a molecular species, then decomposing it under suitable temperature conditions. While successful for many materials, this relied on the formation of the desired product being thermodynamically favorable. It should be noted that the major advantage of the single source precursor approach was not necessarily that it contained the desired elements (because they were always additional unwanted elements, such as carbon and hydrogen) that were removed upon thermolysis, but it was that starting with a molecule ensured a lower activation barrier for solid state diffusion than is required by traditional bulk material synthesis [4]. Furthermore, as an understanding of the mechanistic details increased, it was found to be possible to design single source precursors to form new or meta stable phases [5,6].

Fe–Mo alloys are used extensively in the steel industry to impart desirable properties, such as improved hardening, increased melting temperature, improved weldability, enhanced wear resistance, and improved corrosion resistance [7]. Alloying of molybdenum is typically carried out by powder metallurgy (PM). In this regard, pre-alloyed powders are of great interest, given their superior homogeneity in composition, grain structure, and porosity [8]. Currently, the majority of ferro molybdenum powder is produced via an aluminothermic reaction, where silicon and aluminum metal are used to reduce a mixture of molybdic oxide and iron oxide in the presence

of calcium fluoride or lime [9]. This approach produces ferro-molybdenum particles in the typical size range of microns to millimeters. However, the aluminothermic reaction generates large amounts of slag and dust, inevitably causing environmental issues [10]. By contrast, the gas–solid reduction route offers advantages in the versatility of reduction gases (CH_4, CO, H_2), relatively low processing temperatures, and production of powders with particle size in the micro and nano regime [11]. Nanostructured powder materials exhibit several desirable mechanical qualities, in addition to the desirable PM processing characteristics derived from their inherently high surface area-to-volume properties, such as relatively lower sintering temperature and reduced grain sizes [12]. Preparation of Fe–Mo nanoalloys has been demonstrated by several chemical and physical methods, including thermal decomposition [13], solution phase wet chemical reduction [14], electrochemical synthesis [15], microwave synthesis [16], sonochemical synthesis [17], chemical vapor condensation [18], and high-energy ball milling [19]; however, size and stoichiometric control remains a challenge.

We have previously employed the large molecular cluster, $[H_xPMo_{12}O_{40} \subset H_4Mo_{72}Fe_{30}(O_2CMe)_{15}O_{254}(H_2O)_{98-y}(EtOH)_y]$ (**1**) [20] (Figure 1), as a catalyst precursor for the growth of carbon nanotubes (CNTs) [21–25]. During our study, we demonstrated that the composition of the catalyst, and the subsequent ability to grow CNTs, was highly dependent on the activation step, which involved reduction at elevated temperatures [24]. This, in turn, led to a detailed study of the kinetics of the reduction from **1** to the active catalyst species [26]. Given that **1** is, by definition, a nano-sized precursor (~2.5 nm) with a precise metal composition (Fe/Mo = 30:84) it represents a potential single source precursor for the formation of Fe–Mo alloys.

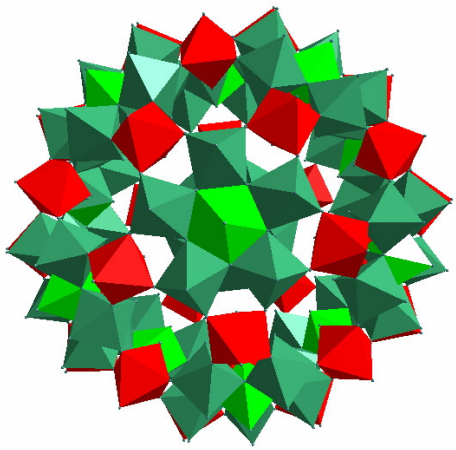

Figure 1. Polyhedral representation of **1** with red and green representing FeO_6 and MoO_6 octahedra, respectively.

2. Materials and Methods

*2.1. $[H_xPMo_{12}O_{40} \subset H_4Mo_{72}Fe_{30}(O_2CMe)_{15}O_{254}(H_2O)_{90-y}(EtOH)_y]$ (**1**) Synthesis*

Compound **1** was synthesized and purified as reported [20,24,25]. In brief, 1.00 g (5.03 mmol) of iron (II) chloride tetrahydrate was dissolved in 75 mL of Millipore water in a 500 mL round-bottom flask containing a stir rod. Afterwards, 2.00 g (8.27 mmol) of sodium molybdate dihydrate, 10 mL (59 mmol) of pure glacial acetic acid, and 2.50 g (1.37 mmol) of phosphomolybdic acid hydrate were added to the flask. The pH of the solution was then adjusted to 2 using HCl, and subsequently stirred for 45 min. The solution was then filtered through a fine glass frit and left to crystallize in air. Afterwards, the crystals were vacuumed filtered and washed with cold DI water. After being dried in air, the solid was placed into a filter thimble and transferred to a Soxhlet extractor. The product was refluxed in EtOH for 12 h and a dark green solution was collected.

2.2. Reduction Experiments

Reduction of **1** was carried out using a TA instruments Q-600 (TMDSC, New Castle, DE, USA) simultaneous thermogravimetric/differential scanning calorimetry (TGA/DSC) system using a carrier gas consisting of air, argon, or a reducing atmosphere (5, 10, or 50% hydrogen with an argon balance). Samples of **1** (ca. 20 mg) were prepared by evaporating 1 mL of a concentrated solution. The samples were then placed in alumina pans and heated with a linear heating rate of 10 °C/min under a carrier gas flow of 70 mL/min.

2.3. Characterization

The scanning electron microscope (SEM) characterization was conducted on a FEI Quanta 400 high-resolution field emission microscope (Thermo Scientific, Hillsboro, OR, USA) equipped with an energy dispersive X-ray spectroscopy (EDX) detector. SEM samples were placed on aluminum SEM stubs, used as received. Images were acquired with a typical operating voltage of 30 kV, with a working distance of 10 mm, and a spot size of 3, under the high vacuum setting. The EDX spectra was acquired with a takeoff angle of 35°, a process time of 7.68 µs, and a 137.5 eV resolution. EDX analysis was performed using the EDAX-TEAM™ software (AMETEK, Inc., Mahwah, NJ, USA). XRD measurements were performed on a Rigaku D/Max Ultima II (Rigaku, The Woodlands, TX, USA) using a Cu Kα radiation source operating at 40 kV and 40 mA. We note that EDX has a detection depth of ca. 1 µm and, thus, only provides analysis up to this depth. However, in order to provide representative analysis, samples were ground, and multiple analyses were taken across the sample. Analysis of the XRD patterns was conducted using Rigaku's PDXL2 software (Version 2.4.2.0; Rigaku, The Woodlands, TX, USA). TEM was conducted using a JEOL 1230 high-contrast transmission electron microscope (JOEL, Peabody, MA USA) at 120 KV equipped with a CCD camera. TEM samples were prepared by drop-casting a dilute solution of **1** (0.1 µM) onto 400-mesh lacey carbon TEM grids (Ted Pella, Inc., Product No. 01824, Redding, CA, USA).

3. Results and Discussion

Synthesis and Characterization of $[H_xPMo_{12}O_{40}{\subset}H_4Mo_{72}Fe_{30}(O_2CMe)_{15}O_{254}(H_2O)_{90-y}(EtOH)_y]$ (**1**)

Compound **1** was synthesized using previously reported method [24,25]. TEM analysis (Figure 2) confirms the nanocluster morphology. Reduction of **1** was carried out in an alumina pan using a thermogravimetric/differential scanning calorimetry (TGA/DSC) system using a carrier gas consisting of 5%, 10%, or 50% hydrogen (Ar balance) with a flow rate of 70 mL/min. The conditions were chosen in view of our previous results that demonstrated that **1** was completely decomposed under air or Ar at 1100 °C, while CNT growth is observed at 900 °C upon decomposition under an atmosphere of 5% H_2 (Ar balance) [24]. Subsequent experiments were aimed at determining the effects of temperature and hydrogen composition. A summary of the experimental conditions is shown in Table 1.

Decomposition of **1** in air at 1100 °C (Air@1100) resulted in the loss of Mo as determined by energy dispersive electron X-ray spectroscopy (EDX), see Table 2. This is confirmed by X-ray diffraction (XRD, see Figure 3), which shows the presence of crystalline Fe_2O_3 as the major product. Both observations are in line with our previous results [24,26]. The low Mo content is proposed to be due to the preferential formation of volatile MoO_3 in preference to a mixed Fe–Mo oxide [24]. Even though the experimental temperature (1100 °C) is nominally below the sublimation temperature of bulk MoO_3 (T_{sub} = 1155 °C), the high surface area and in situ formation is expected to facilitate volatilization [27]. The XRD also shows the presence of crystalline Al_2O_3 and $Al(PO_4)$ as minor products (Table 3), which are most likely incorporated as a result of physical removal of the sample out of the alumina pan. The $Al(PO_4)$ is presumably due to the phosphorous present in the **1** reacting with the alumina of the pan [28].

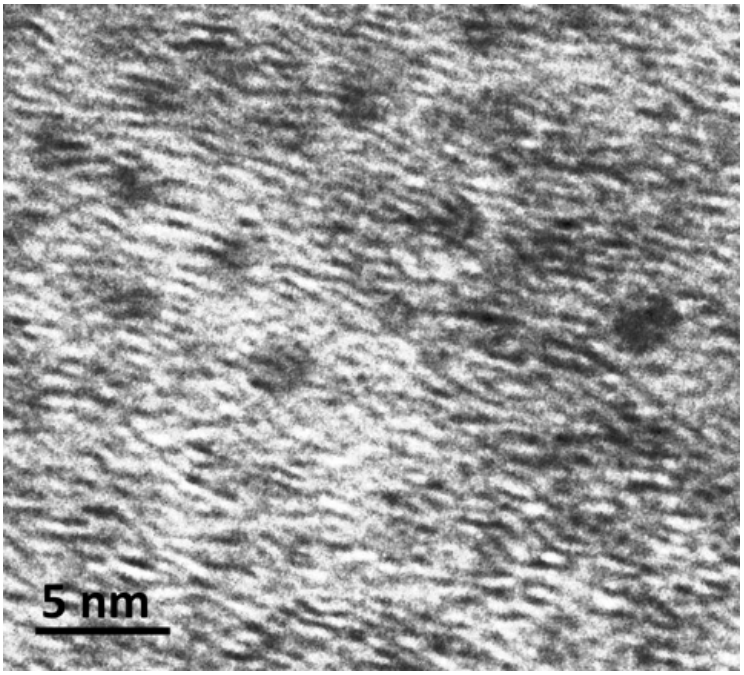

Figure 2. Transmission electron microscopy (TEM) image of **1**.

Table 1. Summary of experimental conditions and acronym used herein.

Experiment	Atmosphere	Temperature (°C)	Acronym
1	Air	1100	Air@1100
2	Ar	1100	Ar@1100
3	5% H_2 (Ar balance)	900	5@900
4	5% H_2 (Ar balance)	1100	5@1100
5	10% H_2 (Ar balance)	1100	10@1100
6	50% H_2 (Ar balance)	1200	50@1200

Table 2. Summary of elemental composition as determined by EDX [a].

Sample	Mo (at %)	Fe (at %)	O (at %)	C (at %)	P (at %)
Air@1100	0.80 ± 0.36	38.98 ± 4.31	47.81 ± 3.89	8.26 ± 0.83	4.15 ± 0.64
Ar@1100	38.42 ± 6.63	9.03 ± 0.51	50.54 ± 6.79	1.24 ± 0.76	0.77 ± 0.12
5@900	31.18 ± 4.28	26.40 ± 3.75	18.17 ± 2.24	20.27 ± 6.21	3.95 ± 1.06
5@1100	64.64 ± 2.65	15.43 ± 2.51	18.50 ± 4.11	0.36 ± 0.35	18.50 ± 4.11
10@1100	65.59 ± 1.54	34.41 ± 1.54	[b]	[b]	[b]
50@1200	76.18 ± 3.75	16.27 ± 2.79	6.42 ± 3.35	[b]	0.84 ± 0.75

[a] Measured across multiple locations in a single sample. [b] Not detected.

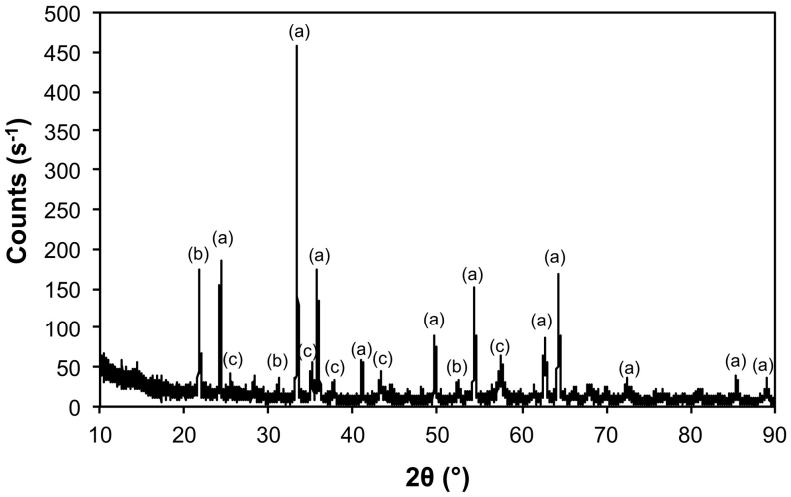

Figure 3. X-ray diffraction (XRD) of the product from the thermal decomposition of **1** under air at 1100 °C (Air@1100) with crystalline phases (Table 3) indicated: (a) Fe_2O_3, (b) $Al(PO_4)$, and (c) Al_2O_3.

Table 3. Summary of crystalline phases detected by XRD and crystallite size, determine from the Scherer equation.

Sample	Phase	ICDD	Crystallite Size (Å)
Air@1100	Fe_2O_3	04-008-7624	963 ± 240
	$Al(PO_4)$	04-015-7505	746 ± 545
	Al_2O_3	01-073-5928	326 ± 45
Ar@1100	Mo	00-004-0809	1160 ± 78
	$Fe_3Mo_3O_8$	04-007-6813	489 ± 99
	MoO_2	01-086-0135	541 ± 104
5@900	Mo	00-004-0809	347 ± 8
	Fe_2Mo_3O	04-005-2530	525 ± 60
	Fe_2Mo_3C	01-083-3017	357 ± 53
5@1100	Mo	00-004-0809	460 ± 21
	$Fe_2Mo_3O_8$	01-070-1726	271 ± 161
	Fe_2Mo_3	00-041-1000	365 ± 166
10@1100	Mo	00-004-0809	533 ± 20
	Fe_3Mo_3C	04-005-3925	605 ± 164
	Mo_2C	04-016-3694	521 ± 141
50@1200	Mo	00-004-0809	620 ± 20
	$Mo_{5.08}Fe_{7.92}$	04-003-7152	333 ± 147

In contrast to decomposition in air, thermolysis under Ar at 1100 °C results in a Mo-rich product, as determined by EDX (Table 2). The Mo/Fe ratio, as measured by EDX, is higher than in the starting **1**, see Figure 4. The XRD shows metallic Mo as the major crystalline phase, with $Mo_3Fe_3O_8$ and MoO_2 as minor phases (Figure 5), consistent with the elemental composition. The average crystallite size for Mo is 1160 Å, while the other phases are significantly smaller (Table 3). Since iron oxides are not volatile, and the acetates tend to decompose into oxides, hence the high Mo content. The range of composition, as determined by EDX (Figure 4), is consistent with a level of compositional inhomogeneity in the samples [29].

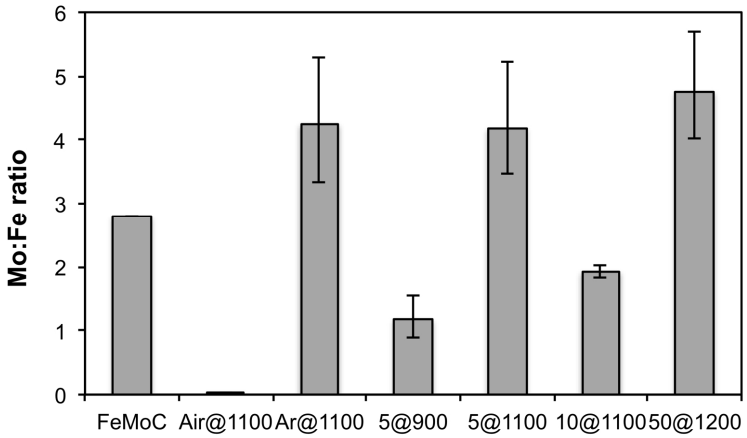

Figure 4. Average Mo/Fe ratio as determined by EDX of the products from the thermal decomposition of **1** under different experimental conditions (Table 1). The error bars indicate the range for multiple measurements across each sample.

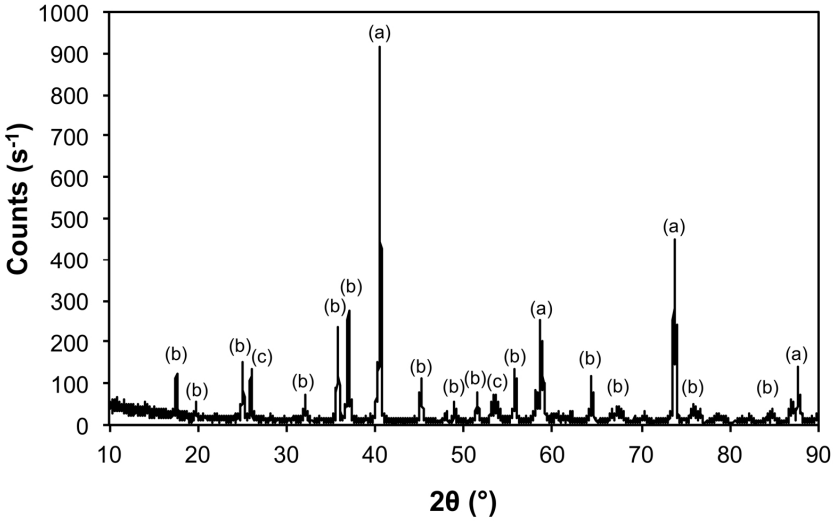

Figure 5. X-ray diffraction (XRD) of the products from the thermal decomposition of **1** under Ar at 1100 °C (Ar@1100) with crystalline phases (Table 3) indicated: (a) Mo, (b) $Mo_3Fe_3O_8$, and (c) MoO_2.

As noted above, decomposition of **1** at 900 °C is the lowest temperature for CNT growth under an atmosphere of 5% H_2 (Ar balance) [24] and, thus, the product represents an active catalyst composition. Based upon EDX analysis (Figure 4 and Table 2) the product (5@900) is Mo deficient as compared to **1**, but not as much as the Air@1100. This observation is consistent with the thermolysis temperature being significantly lower than the sublimation temperature of MoO_3, suggesting only a small amount of Mo is lost during thermolysis. Elemental Mo represents the majority of crystalline components (Table 3). Although minor components of Fe_3Mo_3C and Fe_3Mo_3O are observed (Figure 6) the remaining Fe must be associated with non-crystalline material (presumably Fe_3Mo_3E, where E = O, C). Previously, Fe_3Mo_3C has previously been synthesized by annealing 9 nm sized elemental powders at 700 °C for 70 h, suggesting that crystalline phase formation is slow, even for nm scale composition [30]. SEM analysis shows a relatively smooth morphology composed of fused particulates <1 μm in diameter (Figure 7a,d). The associated EDX map shows a uniform distribution of Mo and Fe (Figure 7a–c), which suggests the crystalline phases are embedded within a Fe–Mo carbide/oxide matrix. It should be noted that 5@900 contains P that is also uniformly distributed through the sample, possibly consistent with the retention of the Keggin core structure of **1**.

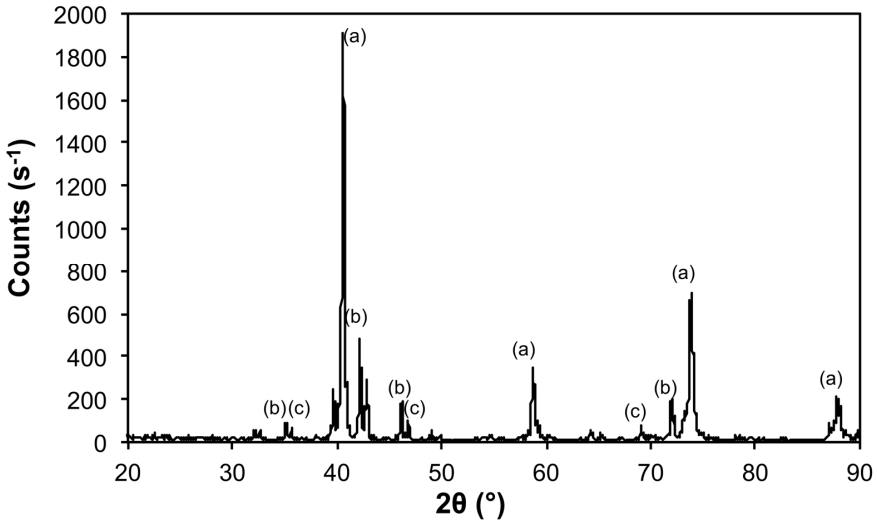

Figure 6. X-ray diffraction (XRD) of the products from the thermal decomposition of **1** under 5% H_2 (Ar balance) at 900 °C with crystalline phases (Table 3) indicated: (a) Mo, (b) Mo_3Fe_3C, and (c) Mo_3Fe_3O.

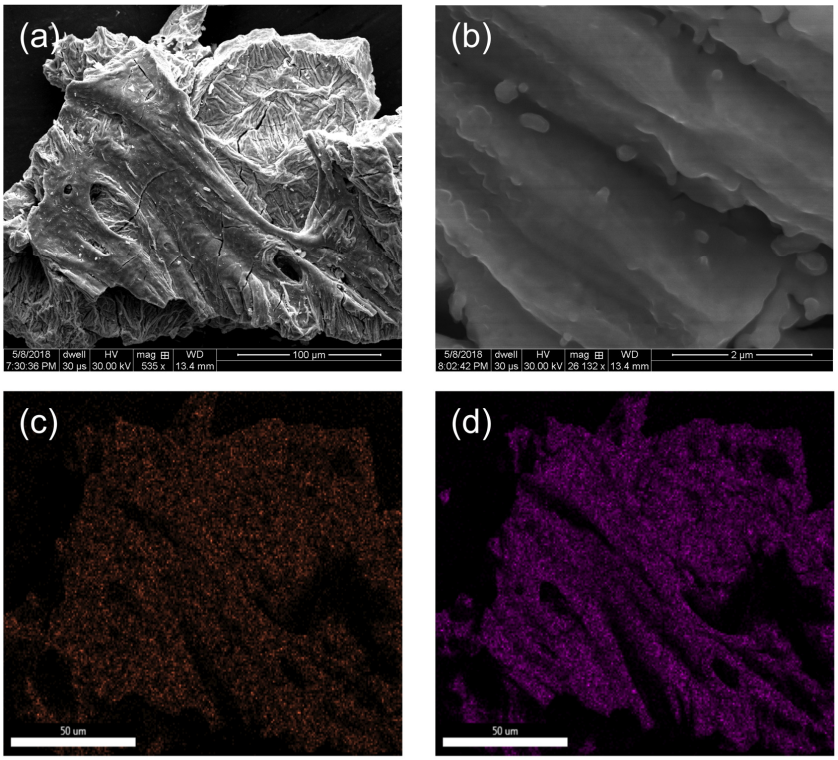

Figure 7. SEM images (**a**,**b**) of the product from thermolysis of **1** at 900 °C under an atmosphere of 5% H_2 (Ar balance), along with the (**c**) Fe and (**d**) Mo EDX maps associated with the SEM image (**a**). Scale bar: (**a**) 100 μm, (**b**) 2 μm, and (**c**,**d**) 50 μm.

Increasing the thermolysis temperature to 1100 °C of the Fe–Mo–C system has previously resulted in the formation of MoOC and Fe_2C [29]. This is not observed for 5@1100. Instead, a Mo-rich composition is formed (Figure 4 and Table 2), whose morphology at higher magnification (Figure 8) is highly porous, and similar to the intermetallic compound Fe_2Mo formed by the H_2 reduction of Fe_2MoO_4 [31] despite the composition being closer to Mo/Fe = 4:1. The crystallinity is dominated by elemental Mo with only low intensity peaks consistent with $Fe_2Mo_3O_8$ (Kamiokite) and, possibly, the intermetallic Fe_2Mo_3 (Figure 9). Certainly, the phases are consistent with the overall Mo-rich

composition, as compared to the precursor (**1**). The EDX map shows a uniform distribution across the sample. As would be expected, the increase in annealing temperature results in an increase in the crystallite size, especially of Mo, as compared to that seen for 5@900 (Table 3).

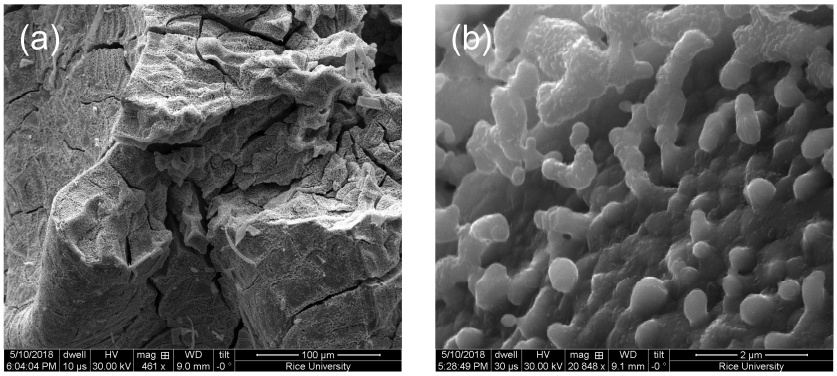

Figure 8. SEM images of the product from thermolysis of **1** at 1100 °C under an atmosphere of 5% H_2 (Ar balance). Scale bar: (**a**) 100 μm and (**b**) 2 μm.

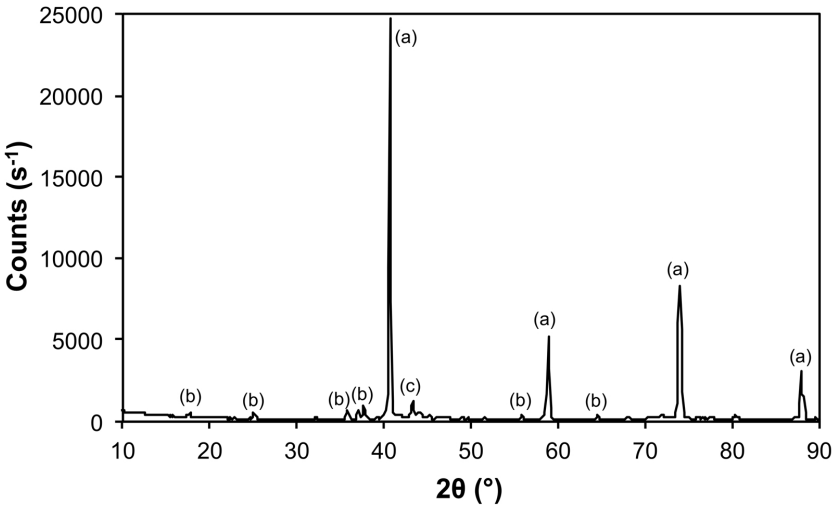

Figure 9. X-ray diffraction (XRD) of the products from the thermal decomposition of **1** under 5% H_2 (Ar balance) at 1100 °C, with crystalline phases (Table 3) indicated: (a) Mo, (b) $Mo_2Fe_3O_8$, and (c) Fe_2Mo_3.

Increasing the H_2 composition to 10% (i.e., 10@1100) results in a sample comprising of fused particles approximately 0.5 μm in diameter (Figure 10), which is comparable to the crystallite sizes as determined from XRD (Table 3). Interestingly, use of a higher H_2 composition resulted in the formation of crystalline intermetallic carbide (Fe_3Mo_3C) and Mo_2C, in addition to elemental Mo (Figure 11). The Mo-rich crystalline phases are consistent with the overall composition being close to Mo_2Fe (Table 2), although this is lower than the precursor (**1**). Despite the crystalline formation of the carbides, the C content is below the reliable detection limit of EDX.

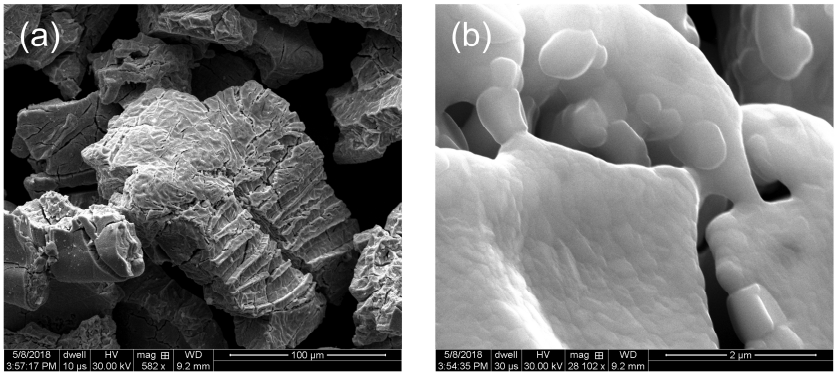

Figure 10. SEM images of the product from thermolysis of **1** at 1100 °C under an atmosphere of 10% H_2 (Ar balance). Scale bar: (**a**) 100 µm and (**b**) 2 µm.

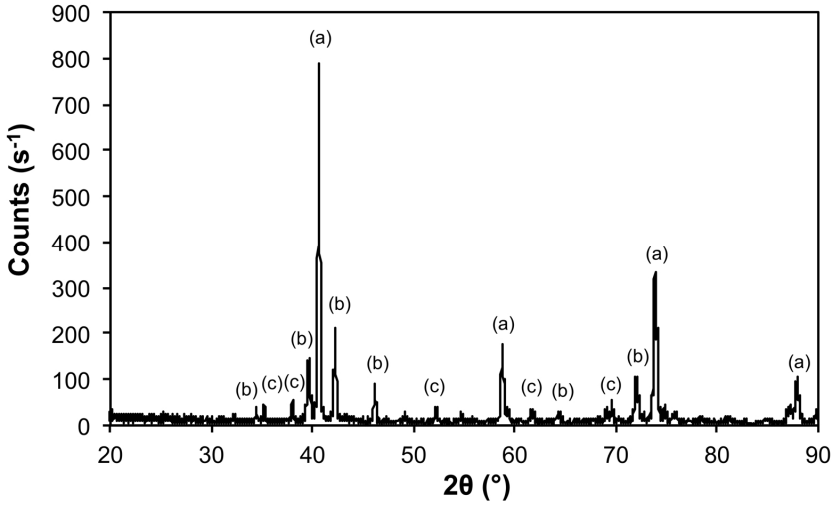

Figure 11. X-ray diffraction (XRD) of the products from the thermal decomposition of **1** under 10% H_2 (Ar balance) at 1100 °C with crystalline phases (Table 3) indicated: (a) Mo, (b) Mo_3Fe_3C, and (c) Mo_2C.

Thermolysis of **1** at 1200 °C under an atmosphere of 50% H_2 (Ar balance) results in an overall composition close to Mo_5Fe (Figure 4 and Table 2). The XRD shows the intermetallic $Mo_{5.08}Fe_{7.92}$ as a minor component in addition to elemental Mo (Figure 12). As befits the higher temperature, the crystallite size for the Mo is increased over that observed for 10@1100 (Table 3). Consideration of the Fe–Mo phase diagram [31] suggests that reduction of **1** at 1200 °C under a highly reducing atmosphere should result in the formation of a composition Fe_xMo_{1-x} (x = 0.26) with a melting point of 1240 °C, which upon cooling, would form a mixture of Mo and $Mo_{0.39}Fe_{0.61}$.

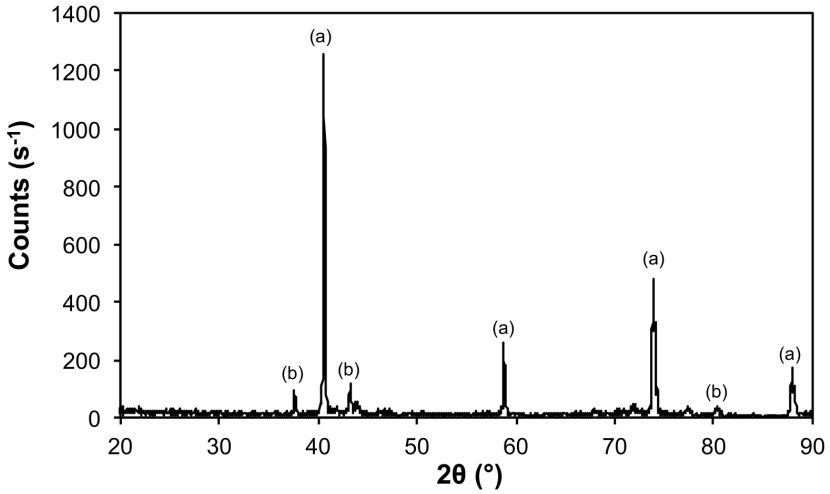

Figure 12. X-ray diffraction (XRD) of the products from the thermal decomposition of **1** under 50% H_2 (Ar balance) at 1200 °C with crystalline phases (Table 3) indicated: (a) Mo and (b) $Mo_{5.08}Fe_{7.92}$.

4. Conclusions

Our results indicate that while compound **1** would appear to be an ideal molecular single source precursor for MoFe alloys, given that it has a defined composition and size, thermolysis under different conditions show that the product elemental and phase composition are highly dependent on the atmosphere and the temperature. These results are in line with our previous results [24,26]. Unfortunately, **1** forms a wide range of compositions during decomposition, with metallic Mo as the major crystalline phase in all samples under reducing atmospheres, probably a consequence of the high overall Mo/Fe ratio. In future, if polyoxometalates (POMs) are to be employed as catalyst precursors for chiral specific CNT growth, then it is important that upon thermolysis, the structure and composition that cannot alter on thermolysis or, alternatively, form a highly stable phase.

Author Contributions: G.L.E. performed all the experiments and characterization. A.R.B. provided guidance to experiments. Both authors contributed to writing the manuscript.

Funding: Financial support for this work is provided by the Robert A. Welch Foundation (C-0002), the NSF IRISE training program at Rice University (NSF HER-0966303), the Welsh Government Sêr Cymru Programme. This work is also supported by the Flexible Integrated Energy Systems (FLEXIS) research operation, and the Reducing Industrial Carbon Emissions (RICE) research operation, both partly funded by the European Regional Development Fund (ERDF).

Conflicts of Interest: The authors declare no conflict of interest.

References

1. Bochmann, M. Metal chalcogenide materials: Chalcogenolato complexes as "single-source" precursors. *Chem. Vap. Depos.* **1996**, *2*, 85–96. [CrossRef]
2. Maury, F. Organometallic molecular precursors for low-temperature MOCVD of III–V semiconductors. *Adv. Mater.* **1991**, *3*, 542–548. [CrossRef]
3. Barron, A.R.; Rees, W.S., Jr. Group 2 compounds as CVD-precursors for electronic materials. *Adv. Mater. Opt. Electron.* **1993**, *2*, 271–288. [CrossRef]
4. Cowley, A.H.; Jones, R.A. Single-source III/V precursors: a new approach to gallium arsenide and related semiconductors. *Angew. Chem. Int. Ed. Engl.* **1989**, *28*, 1208–1215. [CrossRef]
5. MacInnes, A.N.; Power, M.B.; Barron, A.R. Chemical vapor deposition of cubic gallium sulfide thin films: A new meta-stable phase. *Chem. Mater.* **1992**, *4*, 11–14. [CrossRef]
6. Keys, A.; Bott, S.G.; Barron, A.R. MOCVD growth of gallium sulfide using di-*tert*-butyl gallium dithocarbamate precursors: formation of a metastable phase of GaS. *Chem. Mater.* **1999**, *11*, 3578–3587. [CrossRef]

7. Shields, J.A. *Applications of Molybdenum Metal and Its Alloys*; International Molybdenum Association (IMOA): London, UK, 2013.
8. Horn, T.J.; Harrysson, O.L.A. Overview of current additive manufacturing technologies and selected applications. *Sci. Prog.* **2012**, *95*, 255–282. [CrossRef] [PubMed]
9. Belitskus, D. Aluminothermic production of metals and alloys. *JOM* **1972**, *24*, 30–34. [CrossRef]
10. Kim, B.-S.; Kim, S.-B.; Lee, H.-I.; Choi, Y.-Y. A novel process for producing ferromolybdenum powder master alloy without generating secondary pollutants through a two-step hydrogen reduction process. *Mater. Trans.* **2011**, *52*, 1288–1293. [CrossRef]
11. Morales, R. Kinetics of reduction of FeO–Fe_2MoO_4–MoO_2 mixtures toward the production of Fe–Mo alloys. *Scand. J. Metall.* **2003**, *32*, 263–272. [CrossRef]
12. Rajabi, J.; Muhamad, N.; Sulong, A.B.; Fayyaz, A.; Wahi, A. Advantages and limitations of using nano sized powders for powder injection molding process: A review. *J. Teknol.* **2012**, *59*, 137–140.
13. Wanjala, B.N.; Fang, B.; Shan, S.; Petkov, V.; Zhu, P.; Loukrakpam, R.; Chen, Y.; Luo, J.; Yin, J.; Yang, L.; et al. Design of ternary nanoalloy catalysts: effect of nanoscale alloying and structural perfection on electrocatalytic enhancement. *Chem. Mater.* **2012**, *24*, 4283–4293. [CrossRef]
14. Mandal, M.; Kundu, S.; Sau, T.K.; Yusuf, S.M.; Pal, T. Synthesis and characterization of superparamagnetic Ni−Pt nanoalloy. *Chem. Mater.* **2003**, *15*, 3710–3715. [CrossRef]
15. Reetz, M.T.; Helbig, W. Size-selective synthesis of nanostructured transition metal clusters. *J. Am. Chem. Soc.* **1994**, *116*, 7401–7402. [CrossRef]
16. Abdelsayed, V.; Aljarash, A.; El-Shall, M.S.; Al Othman, Z.A.; Alghamdi, A.H. Microwave synthesis of bimetallic nanoalloys and co oxidation on ceria-supported nanoalloys. *Chem. Mater.* **2009**, *21*, 2825–2834. [CrossRef]
17. Mizukoshi, Y.; Fujimoto, T.; Nagata, Y.; Oshima, R.; Maeda, Y. Characterization and catalytic activity of core−shell structured gold/palladium bimetallic nanoparticles synthesized by the sonochemical method. *J. Phys. Chem. B* **2000**, *104*, 6028–6032. [CrossRef]
18. Choi, C.J.; Tolochko, O.; Kim, B.K. Preparation of iron nanoparticles by chemical vapor condensation. *Mater. Lett.* **2002**, *56*, 289–294. [CrossRef]
19. Fecht, H.J.; Hellstern, E.; Fu, Z.; Johnson, W.L. Nanocrystalline metals prepared by high-energy ball milling. *Metall. Trans. A* **1990**, *21*, 2333–2337. [CrossRef]
20. Müller, A.; Das, S.K.; Kögerler, P.; Bögge, H.; Schmidtmann, M.; Trautwein, A.X.; Schunemann, V.; Krickemeyer, E.; Preetz, W. A new type of supramolecular compound: Molybdenum-oxide-based composites consisting of magnetic nanocapsules with encapsulated keggin-ion electron reservoirs cross-linked to a two-dimensional network. *Angew. Chem. Int. Ed.* **2000**, *39*, 3413–3417. [CrossRef]
21. Anderson, R.E.; Colorado, R., Jr.; Crouse, C.; Ogrin, D.; Maruyama, B.; Pender, M.J.; Edwards, C.L.; Whitsitt, E.; Moore, V.C.; Koveal, D.; et al. A study of the formation, purification, and application as a SWNT growth catalyst of the nanocluster [$H_xPMo_{12}O_{40}$⊂$H_4Mo_{72}Fe_{30}(O_2CMe)_{15}O_{254}(H_2O)_{98}$]. *Dalton Trans.* **2006**, 3097–3107. [CrossRef] [PubMed]
22. Ogrin, D.; Anderson, R.E.; Colorado, R., Jr.; Maruyama, B.; Pender, M.J.; Moore, V.C.; Pheasant, S.T.; McJilton, L.; Schmidt, H.K.; Hauge, R.H.; et al. Amplification of single walled carbon nanotubes from designed seeds: separation of nucleation and growth. *J. Phys. Chem. C* **2007**, *111*, 17804–17806. [CrossRef]
23. Ogrin, D.; Barron, A.R. Coordination chemistry of the nanocluster [$H_xPMo_{12}O_{40}$⊂$H_4Mo_{72}Fe_{30}(O_2CMe)_{15}O_{254}(H_2O)_{98}$]. *J. Clust. Sci.* **2007**, *18*, 113–120. [CrossRef]
24. Esquenazi, G.L.; Barron, A.R. Understanding the "activation" of the nanocluster [$H_xPMo_{12}O_{40}$⊂$H_4Mo_{72}Fe_{30}(O_2CMe)_{15}O_{254}(H_2O)_{98-y}(EtOH)_y$] for low temperature growth of carbon nanotubes. *J. Clust. Sci.* **2018**, *29*, 431–441. [CrossRef]
25. Esquenazi, G.L.; Brinson, B.; Barron, A.R. Catalytic growth of carbon nanotubes by direct liquid injection CVD using the nanocluster [$H_xPMo_{12}O_{40}$⊂$H_4Mo_{72}Fe_{30}(O_2CMe)_{15}O_{254}(H_2O)_{98-y}(EtOH)_y$]. *C* **2018**, *4*, 17. [CrossRef]
26. Esquenazi, G.L.; Barron, A.R. Reduction kinetics of the nanocluster [$H_xPMo_{12}O_{40}$⊂$H_4Mo_{72}Fe_{30}(O_2CMe)_{15}O_{254}(H_2O)_{98-y}(EtOH)_y$]. *J. Clust. Sci.* **2018**, *29*, 325–335. [CrossRef]
27. Gulbransen, E.A.; Andrew, K.F.; Brassart, F.A. Oxidation of molybdenum 550 °C to 1700 °C. *J. Electrochem. Soc.* **1963**, *110*, 952–959. [CrossRef]

28. Gonzalez, F.J.; Halloran, J.W. Reaction of orthophosphoric acid with several forms of aluminum oxide. *Am. Ceram. Soc. Bull.* **1980**, *59*, 727–731.
29. Fahlman, B.D.; Bott, S.G.; Barron, A.R. An accuracy assessment of the refinement of partial metal disorder in solid solutions of $Al(acac)_3$ and $Cr(acac)_3$. *J. Chem. Soc. Dalton Trans.* **2001**, 2148–2152. [CrossRef]
30. Zakeri, M.; Rahimipour, M.R.; Khanmohammadian, A. Mechanically activated synthesis of nanocrystalline ternary carbide Fe_3Mo_3C. *Mater. Sci. Eng. A* **2008**, *492*, 311–316. [CrossRef]
31. Morales, R.; Arvanitidis, I.; Sichen, D.; Seetharaman, S. Reduction of Fe_2MoO_4 by hydrogen gas. *Metall. Mater. Trans. B* **2002**, *33*, 589–594. [CrossRef]